Computational assessment of ratcheting in rail-wheel contact with solid contaminant

Angelo Mazzù [*], Davide Battini , Nicola Zani

University of Brescia, Department of Mechanical and Industrial Engineering, Via Branze, 38, 25123, Brescia, Italy

A B S T R A C T

A numerical method for the fast evaluation of ratcheting in solid-contaminated contact between rollers was developed. The physical problem was simplified with a plane-strain half-infinite body, with a distribution of pressure and tangential stress on the contact surface obtained by considering the presence of evenly spaced solid contaminant particles between the contacting bodies. Such a distribution was obtained by an analytical method, which considered the material of the contacting bodies as linear elastic. The stresses under the contact surfaces were calculated using the Boussinesq-Cerruti model. Subsequently, the plastic strain accumulated in the roller after each application of the contact load was calculated by means of a non-linear kinematic-hardening constitutive law, also considering the effect of wear in removing material layers from the surface.

First, the effects of the introduced approximations were evaluated. In particular, the error in calculating the plastic strain using contact load distributions from a theory based on linear elastic behavior was evaluated by comparison with the results of finite element models. Subsequently, the method was used to assess the experimental results of previously published studies on sand-contaminated contact between rail and wheel materials. Despite the approximations and indetermination of some model constants, the method was proven to be able to qualitatively explain many of the damage mechanisms related to the interaction of the contacting bodies with the contaminant particles.

1. Introduction

Solid contaminants are often present at the wheel-rail interface and significantly affect their damage. Sand is the most common solid contaminant: its presence can be undesired but unavoidable, such as when railways cross desertic environments [1–3], or intentional, when sand is used to increase the coefficient of friction in slopy wet tracks [4–9]. Another solid contaminant can be the wear debris, detached from the rail and wheel surfaces in condition of poor lubrication, owing to their reciprocal oxidative wear [10]. In particular, Zhou et al. [11] found that, in condition of low slippage, wear was mild and mainly oxidative, and the wear debris looked like a powder. Increasing the slippage, the damage changed in a complicated mechanism including oxidative, fatigue and slightly abrasive wear. Increasing again the slippage, wear changed to severe, driven by ratcheting, delamination and abrasion, due to the formation of large size particles.

The effects of solid contaminants are usually severe, including hollow wear, which alters the correct shape coupling between the wheel and rail [2], and a dramatic durability reduction of both the wheel and rail [16]. Understanding the interaction mechanism between contaminant particles and the wheel-rail system is useful for managing the operation and preventing severe damage in the presence of solid contaminants.

Several studies have been conducted on the experimental side. Some authors [4–6,12–15] highlighted the effectiveness of sand in recovering the required adhesion when liquids and leaves at the contact interface reduce the adhesion coefficient. Grieve et al. [16] showed that the main damage mechanisms leading to these effects are abrasion and indentation by the contaminant particles, and ratcheting due to the adhesion between the wheel and the rail. Ratcheting occurs when the cyclic loading leaves residual deformations at each cycle, which accumulate cycle by cycle. In contact, such behavior is usually related to traction or friction at the contact surface, which tend to elongate the grains along the rolling direction. When the accumulated plastic strain exceeds the critical value, surface cracks oriented as the strain bands can nucleate. A schematic of the ratcheting and crack nucleation mechanism is given in Fig. 1.

Grieve et al. [16] highlighted that these two mechanisms compete because the plastic strain accumulation near the surface is mitigated by

Nomenclature

|	
f	Coefficient of friction
k [MPa]	Shear yield stress
r_p [mm]	Radius of contaminant particles
x [mm]	Coordinate along rolling direction
z [mm]	Coordinate orthogonal to rolling direction
C [MPa]	Material constant for the Chaboche-Lemaitre strain hardening model
P [N]	Contact load
γ	Material constant for the Chaboche-Lemaitre strain hardening model
γ_{xz}	Accumulated plastic strain
λ [mm]	Spacing between contaminant particles
σ_x [MPa]	Normal stress in rolling direction
σ_{yc} [MPa]	Cyclic yield stress
τ_a [MPa]	Alternated shear stress in a load cycle (half range)
τ_{xzmax} [MPa]	Maximum shear stress in a load cycle
τ_{xzmin} [MPa]	Minimum shear stress in a load cycle
$\Delta\gamma_{xz}$	Residual plastic strain at a single load cycle
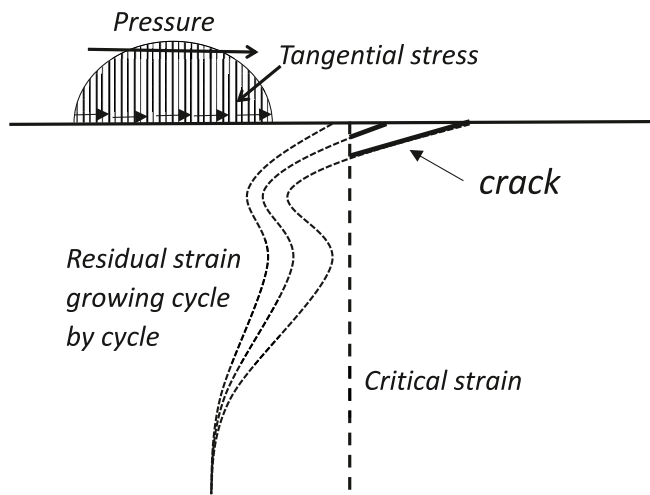
Fig. 1. Schematic of the ratcheting and crack nucleation process.

material removal by wear due to the rolling-sliding contact conditions. Gallardo-Hernandez & Lewis [17] found that applying sand generates indentation in the softer material and abrasion in the harder one: this happens because the hard contaminant particles easily indent the softer material and are embedded in it; once this happens, the softer body becomes similar to a grinding wheel, which scratches and abrades the harder one. Arias-Cuevas et al. [4] studied the effect of the contaminant particle size and found that as the particle size increases, ratcheting increases as well, involving a deeper layer; on the other hand, they did not find a clear influence of the particle size on the wear rate. Shi et al. [18] made experiments with various kinds of solid and liquid contaminants: among other results, they found that the presence of dry sand with large particles increases wear and ratcheting. This was attributed to the particle crushing during the contact, which induces indentation and ratcheting in the contacting bodies. When the contact interface is contaminated with slurries of water and pulverized sand, wear and ratcheting are lower than in the previous case, because of the reduced effect of crushing and indentation. However, the damage increases as the solid fraction in the slurry increases: this was attributed both to water that, when entrapped and pressurized inside the cracks, promotes

their propagation, and to the entrapped solid particles, which act as stress concentrators.

The extensive experimental work on this topic highlighted the need of deepening the understanding of the interaction mechanism between the contaminant particles and the contacting bodies, to improve the resistance of rails and wheels to the detrimental effects of solid contamination. In particular, ratcheting is especially important because it is the driving mechanism of many damage phenomena in wheel-rail contact. To approach this goal, Faccoli et al. [2] first modelled by Finite Elements (FE) the interaction of two contacting and rolling bodies with two solid particles passing through the contact interface. They built a two-dimensional model with plastic materials for the main contacting bodies and elastic material for the contaminant particles, and assigned typical wheel and rail steel constitutive laws to the materials of the main bodies. They found that the stress and strain fields under the contact surface are characterized by two distinct layers: one of large plastic strains on the scale of the particle-body contact area, and the other of moderate strain on the scale of the wheel-rail contact area. A further step was done by Mazzù et al. [19,20], who studied by FE the wheel-rail contact with the contacting bodies fully separated by a number of particles at the interface. Two-dimensional models with plastic bodies and elastic particles were built, and different wheel-rail material couplings were simulated. The results showed that, in the presence of solid contaminants, the plastic strain of each material is scarcely influenced by the properties of the material of the coupled body. In addition, they found that ratcheting could be confined to a layer on the size scale of the particles by increasing the cyclic yield stress of the wheel and rail steel.

To increase the calculation speed in solid contaminated contact, even allowing the repetition of many load cycles, Mazzù & Battini [21] elaborated an analytical model to determine the pressure distribution at the wheel-rail interface in the presence of solid contaminant. Again, such a model is two-dimensional, based on an elastic wheel and rail materials, and rigid contaminant particles. The contact pressure distribution is modelled as a sequence of local Hertz distributions at the particle-body scale, whose peaks vary on the scale of the contact area between the main bodies. By calculating the subsurface stresses under such distributions, the authors could identify the depth of the layer where the stresses are influenced by the particle-body contact, which is approximately three times the particle radius.

In this study, the abovementioned model for the pressure distribution calculation [21] was used to predict ratcheting in a solid-contaminated contact. First, since these pressure distributions are based on elastic wheel and rail materials, the modelling error is evaluated by comparing the results with those obtained by FE models with plastic materials. Then, the pressure distributions are used as input in a fast numerical method based on non-linear kinematic hardening material for the main body, which can simulate the ratcheting occurring after applying many load cycles. The effects of the influencing parameters on particle size, particle distribution, and material properties were investigated.

2. Computational method

2.1. Description

The pressure distribution on the contact surface in the presence of solid contaminant was obtained by the analytical method of Mazzù & Battini [21]. This method allows the determination of the contact forces between the particles and main bodies (wheel and rail) under the following simplifying hypotheses.

- the strain field is plane;
- the solid contaminant particles are rigid, evenly sized and distributed along the contact patch;
- the wheel and rail materials are linear and elastic (only for the pressure distribution calculation).
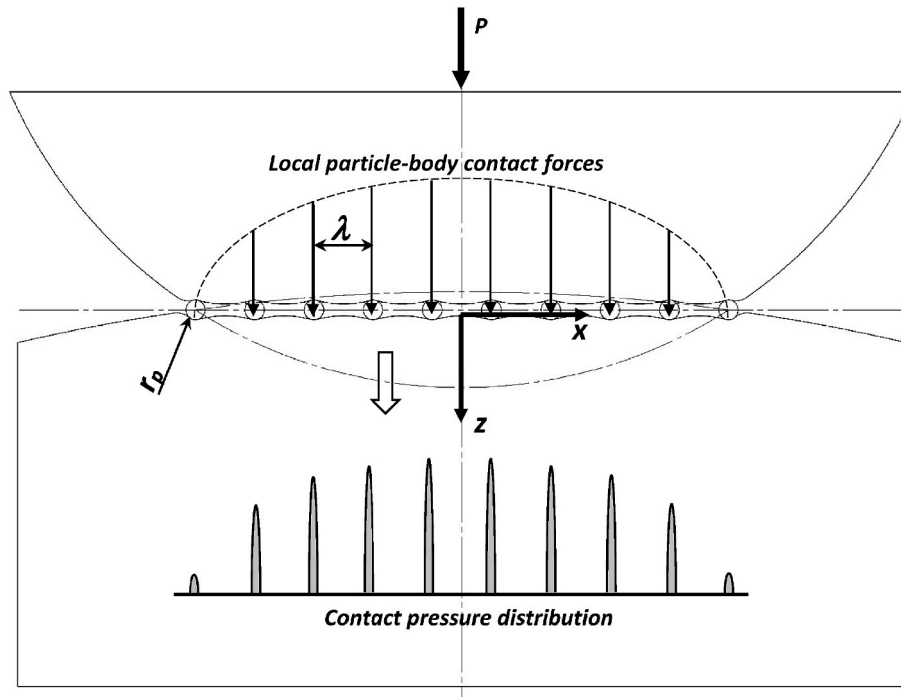
Fig. 2. Schematic of plane strain contact model with solid contaminant.

Once the contact forces between the particles and the main bodies are determined, the local pressure distribution at the interface between each particle and the main bodies can be calculated according to the Hertz model, which refers to rigid or linear elastic contacting bodies. The overall contact pressure distribution depends on the particle radius r_p and spacing λ, the geometry and the elastic constants of the rail and wheel materials, as well as on the total contact load P, as schematically shown in Fig. 2.

Once the pressure distribution has been calculated, the stress field under the subsurface can be obtained according to the Boussinesq-Cerruti model, by adding a tangential stress distribution proportional to the pressure by the coefficient of friction f. This assumption is strictly valid only for pure slip, e.g. with high creepage; however, only for the subsurface strain calculation, it can be extended as an acceptable approximation even for low creepage. Subsequently, considering the distribution as moving along the x direction on the contact surface, the plastic strain increment $\Delta\gamma_{xz}$ during a repetition of a load cycle can be obtained according to the model of Chaboche-Lemaitre in the simplified form of Mazzù for kinematic hardening [22,23]:

$$\Delta\gamma_{xz} = \frac{\sqrt{3}}{\gamma}\ln\left[\frac{\left(\frac{c}{\gamma}\right)^2 - 3(\tau_{xzmin}+k)^2}{\left(\frac{c}{\gamma}\right)^2 - 3(\tau_{xzmax}-k)^2}\right] \tag{1}$$
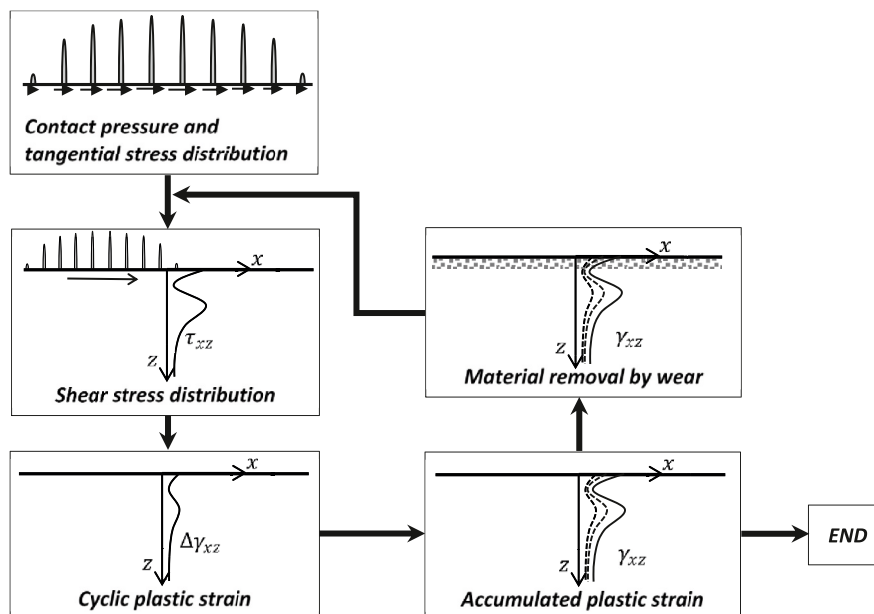

Fig. 3. Flow chart of the plastic strain calculation algorithm.
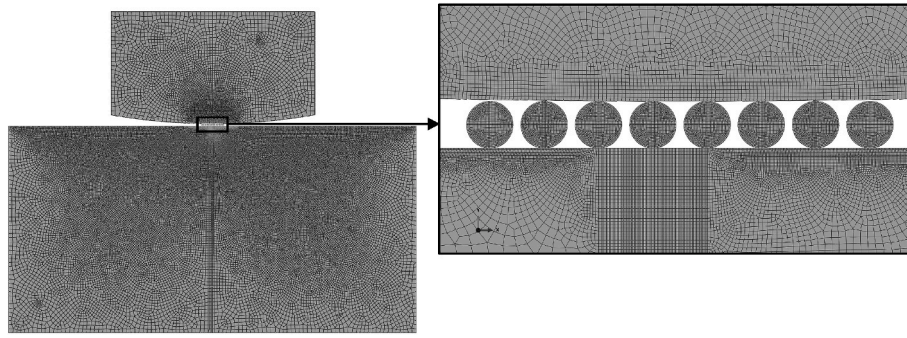
Fig. 4. FE model of the solid-contaminated contact.

where C and γ are material properties, k is the material shear yield stress, and τ_{xzmin} and τ_{xzmax} are the minimum and maximum shear stress during the load cycle, respectively.

This model is applicable to a plane strain case and considers the orthogonal shear strain γ_{xz} as the unique factor responsible for plastic flow. This assumption is based on the evidence that, unless in a shallow surface layer, γ_{xz} is the sole strain component that can accumulate indefinitely for a high cycle number; the other components, in fact, being always compressive during a load cycle, would cause the volume to collapse if accumulated. In the surface layer, this assumption is no longer valid because the σ_x can also show a sign inversion during a load cycle: for that layer, in Ref. [23] a correction of the algorithm was proposed, in order to take into account the role of σ_x in the strain history.

This model can simulate the strain history of several load cycles while considering the effects of wear-removing material layers from the surface. The accumulated plastic strain is calculated periodically along the depth z, and as long as the load repetitions proceed, the stress field is updated to consider the shift of the subsurface layers towards the surface, as an effect of the material layer removal by wear, which is introduced as an external datum. A flowchart of the strain-calculation algorithm is shown in Fig. 3.

2.2. Evaluation of the pressure distribution approximation

The model incorporates several idealized assumptions about the phenomena it represents. A key assumption is that the pressure distribution model is based on the contacting bodies behaving elastically, which merits further investigation as detailed later. Simplifications also extend to the model's dimensionality and geometry, including assumptions of plane strain, uniform size and spacing of sand particles, their circular shape, and a limited number. Further, the model simplifies contaminant behavior by assuming particles are rigid and unbreakable, and it models tangential load as mere friction, omitting the impact of surface roughness. The primary goal of the model, however, is not to precisely detail the interactions at the particle level. Rather, its aim is to provide a general understanding of damage mechanisms, involved material layers, and key influencing factors. This is achieved by evaluating average conditions, which can be determined by analyzing or controlling the typical characteristics of solid contaminants during operational scenarios, as exemplified in the work of Shi et al. [24] and Lewis et al. [25]. Below a certain depth, the model simplifications listed above are assumed to have negligible effects in determining the general material response to repeated solid-contaminated contact loads.

As for the stress and strain calculations, the fact that the plastic strains are calculated from a stress distribution obtained with the model of Bussinesq-Cerruti, which assumes elastic material properties, could appear as an inconsistency. However, it was shown in various papers, even dating back to the Eighties [26,27], that the elastic stress distribution can be used for calculating the cyclic plastic strain to obtain an accurate result.

Table 1
Geometry and load parameters in the FE model.

Disc radius [mm]	Contact load per unit thickness [N]	Nominal contact pressure [MPa]	Nominal contact width [mm]	Particle radius r_p [μm]	Particle spacing λ [μm]
15	503.8	1100	0.29	30-45-60	70-100-130

However, in this study, as mentioned before, the focus was on the use of the analytical pressure distribution, which is based on a theory for linear and elastic bodies, as an input datum for plastic strain calculation. The cited paper of Mazzù & Battini [15] showed that this procedure effectively determines the depth of the layer influenced by the local stresses around the contaminant particles. However, to better define the limit of applicability of this method, Finite Element (FE) models simulating some cases of solid-contaminated contact with elastic-plastic bodies were realized as a benchmark.

As a case study, a modelization of the experimental tests described by Faccoli et al. [2] was performed, in which disc-shaped samples realized with various wheel materials were placed in sand-contaminated contact with discs in the rail material under rolling and sliding conditions. In those experiments, the geometrical parameters differed from real wheel-rail contact conditions, being small-scale tests. In the FE models, such a condition was simulated with a disc in rail material against a flat block in wheel material, with the disc radius equal to the Hertz equivalent radius of the real disc-to-disc coupling to obtain the same nominal contact area and Hertz pressure. To simulate the effect of the solid contaminant size, various values of the particle radius r_p were taken into account; the spacing λ was such to have a distance of 10 μm between the external surfaces of two neighboring particles. The mesh size was refined correctly close to the contact region. Fig. 4 and Table 1 summarize the model parameters; the quantities referred to as "nominal" in
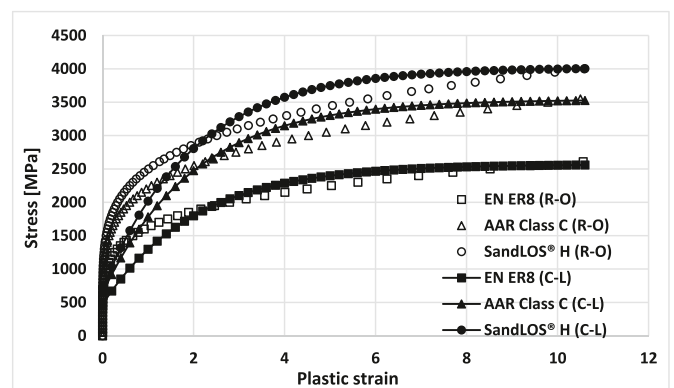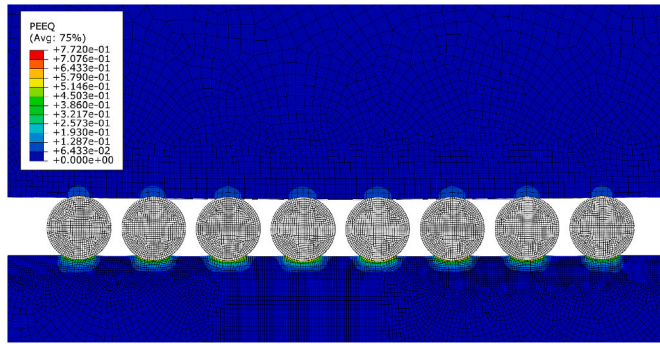

Fig. 5. Constitutive law of the materials used in the simulations.

Table 2
Properties of the wheel and rail materials in the simulations.

Material	Elastic modulus [MPa]	Coefficient of Poisson	Cyclic yield stress σ_{yc} [MPa]	C-L constant C [MPa]	C-L constant γ
EN ER8	206000	0.29	470	1050	0.5
AAR Class C	206000	0.29	650	1450	0.5
SandLOS® H	206000	0.29	700	1650	0.5

Fig. 6. Equivalent plastic strain (PEEQ) map on the deformed FE model with the wheel in EN ER8 wheel steel and particle radius $r_p = 30\ \mu m$. The upper body is in rail material, the lower one in wheel material.

Table 1 are calculated according to the Hertz theory without solid contaminant.

The material of the particles was set as linear elastic, with an elasticity modulus equal to 10^3 times the elasticity modulus of the materials of the main bodies, such to be considered substantially rigid. As the wheel and rail materials are concerned, their constitutive law was given in Ref. [19] in terms of the Ramberg-Osgood (R–O) model; however, to fit the computational method discussed in the present paper, the R–O model was approximated with a Chaboche-Lemaitre (C-L) constitutive law. As the two models can give rather different results depending on the strain amplitude order, it was preferred to have a better approximation for large strain, typical of the wheel-rail contact problem, to be simulated. Given the similar material properties, the same constitutive law of the AAR Class C wheel steel was assumed, even for rail steel. In Fig. 5, the used C-L models are compared with the corresponding R–O models, whereas in Table 2, the corresponding C and γ constants of the C-L model are given.

Fig. 6 shows the deformed model with the equivalent plastic strain (PEEQ) map in the contact zone, with the wheel in EN ER8 steel and $r_p = 30\ \mu$m. The plasticized regions of the wheel material near the particles can be clearly identified. In this region, the deformed wheel material tends to envelop the particles.

Fig. 7 shows the contact pressure as computed by the FE solver with the three materials and particle sizes considered, compared with the analytical pressure distributions. In all cases, the FE pressure distribution was significantly different from the analytical distribution: the local pressure near the particles was distributed over a larger area, was almost flat except for two peaks at the borders, and was much lower than the analytical pressure. The difference between the FE and analytical pressures decreases as the plastic material parameters σ_{yc} and C increase, for example as the material strength and hardening increase.

To investigate the error caused by the analytical pressure distributions, simulations of cyclic plasticity were carried out with the calculation algorithm shown in Fig. 3, using both the analytical pressure distributions and the distributions obtained as output from the FE models as inputs. In addition, the tangential stress distributions were added, by multiplying the pressure distributions by the friction coefficient $f = 0.3$. For each material and particle size, 100 load passages without wear were simulated.

Fig. 8 shows the alternated shear stress $\tau_a = (\tau_{xzmax} - \tau_{xzmin})/2$ along the depth for the three considered particle sizes, calculated according to the Boussinnesq-Cerruti model. For each particle size, the stresses obtained using the analytical pressure distribution were compared with those obtained using the FE pressure distributions. The curves tend to diverge only for an approximate depth of $z < r_p$ and the curves obtained with the analytical pressure distributions are the upper bound. For the curves obtained with the FE pressure distributions, the higher the material parameters σ_{yc} and C, the lower the difference with respect to the upper bound. For $z > r_p$, the difference between the curves tends to be negligible.

Fig. 9 shows the cyclic plastic strain increment along the depth for all the materials and particle sizes considered. The upper and lower diagrams focus on the surface and subsurface layers, respectively. The curve obtained using the analytical pressure distribution for each material and particle size was compared with the corresponding curve obtained using the FE pressure distribution. As expected, the results obtained with the different pressure distributions tended to diverge close to the surface layer because of the difference in the stresses, with the analytical pressure distribution causing a much higher strain. Again, the difference tends to decrease with higher material strength and hardening. In the subsurface layer, for a depth $z > r_p$, the difference between the results obtained with the analytical and FE pressure distributions tends to be reduced. The agreement between the results increased as far as the material parameters σ_{yc} and C, as well as the particle radius r_p, increase. These results suggest that, as a rule of thumb, using the analytical pressure distributions for calculating the cyclic plastic strain gives sufficiently accurate results in the subsurface layer, approximately under a depth equal to the particle radius; this is also coherent with the De Saint Venant principle. However, the results obtained with materials with low strength and hardening should be handled with care. In the surface layer, e.g for $z < r_p$, the plastic strain field calculated with the analytical pressure distributions is largely overestimated. However, this inaccuracy usually has no physical implications in the study of the real cases: indeed, in the surface layer large plastic strain accumulates very rapidly, so that the slope of the deformed fibers tends to be horizontal, corresponding to an accumulated plastic strain $\gamma_{xz} = \infty$. In the numerical simulations, such a condition is represented by a very large γ_{xz} value, if compared with the strain field in the subsurface layer, and is reached in a very few cycles with both the analytical and FE pressure distributions, despite the difference (even of a magnitude order) between the respective cyclic plastic strain increment. In addition, the surface layer is often removed by wear, so it is irrelevant for the final result.

3. Examples of application

In order to verify the effectiveness of the method in the assessment of damage in solid-contaminated wheel-rail contact, it was used to evaluate some published results of small-scale experiments of wheel-rail contact with sand contamination. The evaluation must be intended as qualitative because many input variables are unknown. In particular, the material constants for the Chaboche-Lemaitre model used in the following examples are unknown and their value can only be reasonably estimated. In addition, the size and distribution of the sand particles can also only be estimated since these parameters are random, and even when a size distribution of the sand before the experiments is available, it is not known which particles will be broken during the contact and which ones will be not. Nevertheless, the model can capture the trends and explain the main damage phenomena related to ratcheting.
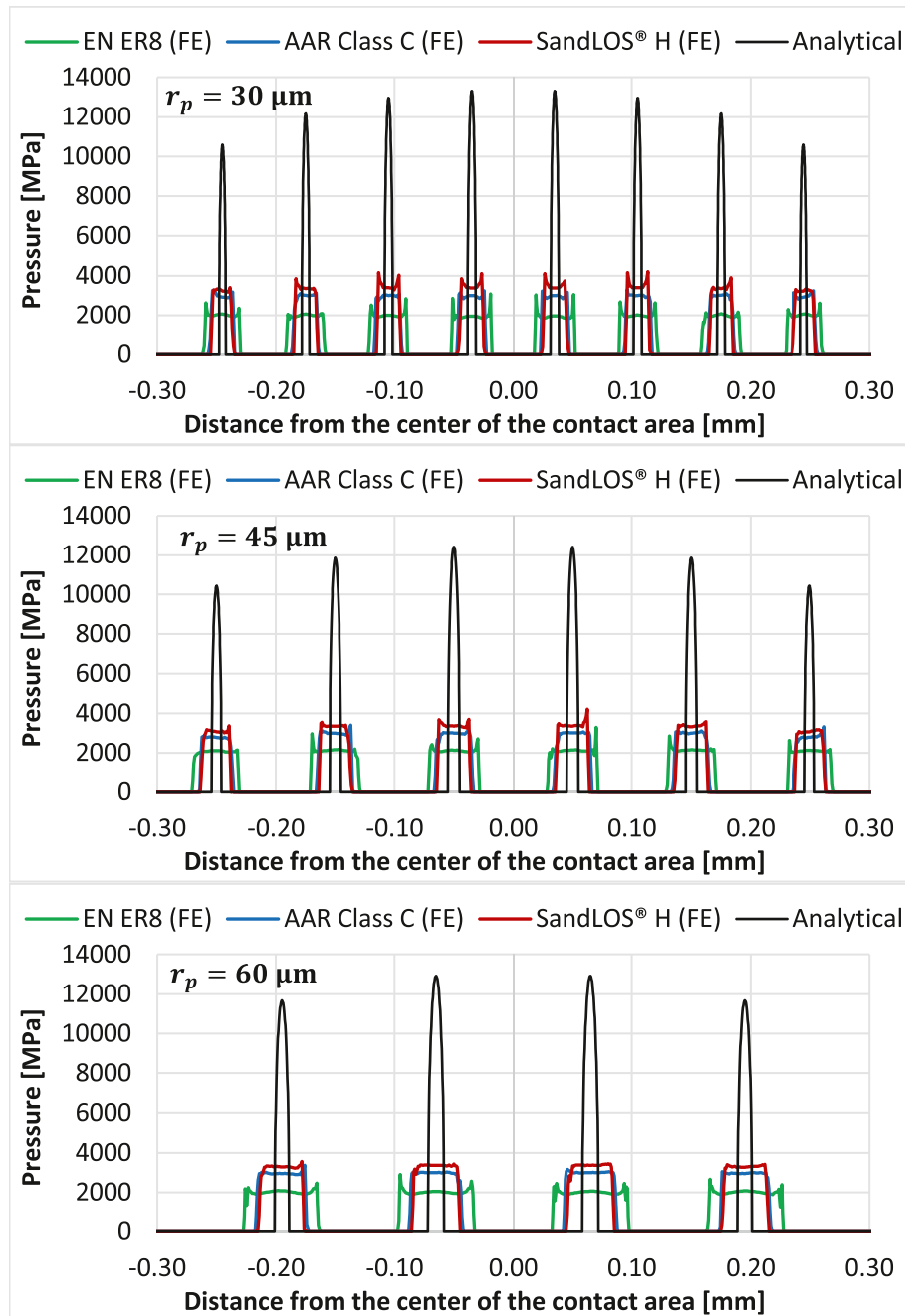
Fig. 7. Pressure distributions for the three particle radii considered, calculated by the FE models with elastic-plastic materials for the main bodies, compared with the analytical distributions according to the theory for elastic materials.

3.1. Effect of the wheel material

The first example of application is the test campaign done by Faccoli et al. [2] on four different wheel materials, e.g. the same as in the previous section (EN ER8, AAR Class C, and SandLOS® H), plus the Sand-LOS® S, which is an improved AAR Class C steel. In those experiments, discs obtained from actual wheels, made with the four steels, were coupled with the same rail steel. All the experiments were carried out with the same contact pressure and rolling/sliding speed, with the addition of a sand flow at the contact interface; experiments in non-contaminated contact were also done for comparison.

To evaluate the effect of varying material properties, the present model assumed the same material constants as the previous section, treating SandLOS® S properties as equivalent to those of Class C. It has

to be underlined that in contact problems, as shown by Mazzù et al. [28], an accurate calibration of the material constants should be based on the results of contact tests. For comparative purposes in this paper, the constants were calibrated based on available data from alternated tension-compression tests.

In [2], the wear rate and the coefficient of friction varied from one test to another; however, in this paper, constant average values were assumed to isolate the effects related to the material properties and to the presence/absence of the solid contaminant.

The particle size was unknown; the results of the experiments done by Grieve et al. [16] were considered to estimate an average value. In those experiments, the authors measured the particle size distribution before and after the contact with the specimens. The number of particles whose diameter was lower than 60 μm increased when passing through
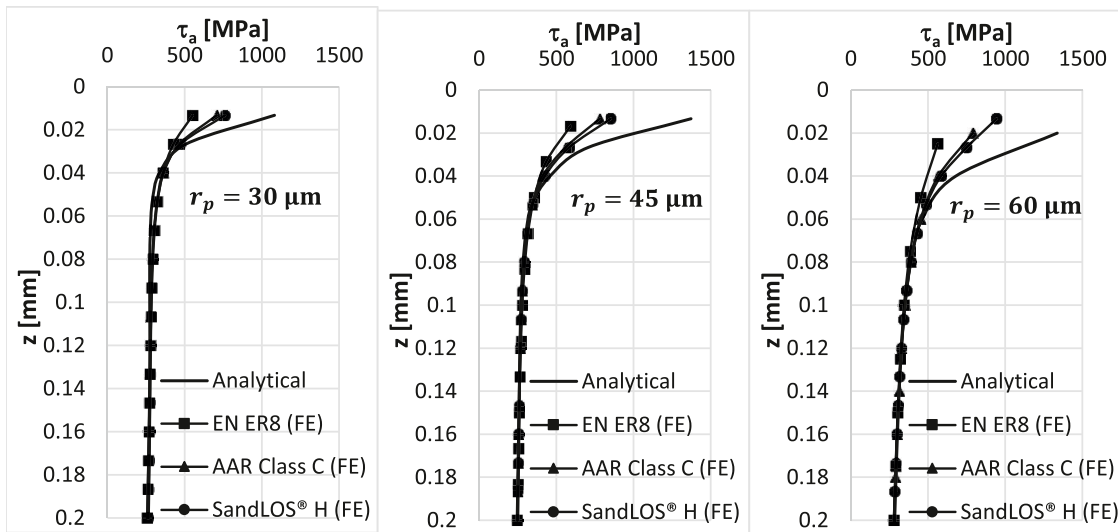
Fig. 8. Alternated shear stress along the depth with varying particle size, calculated with the analytical pressure distributions and with the pressure distributions obtained by the FE models with plastic materials.
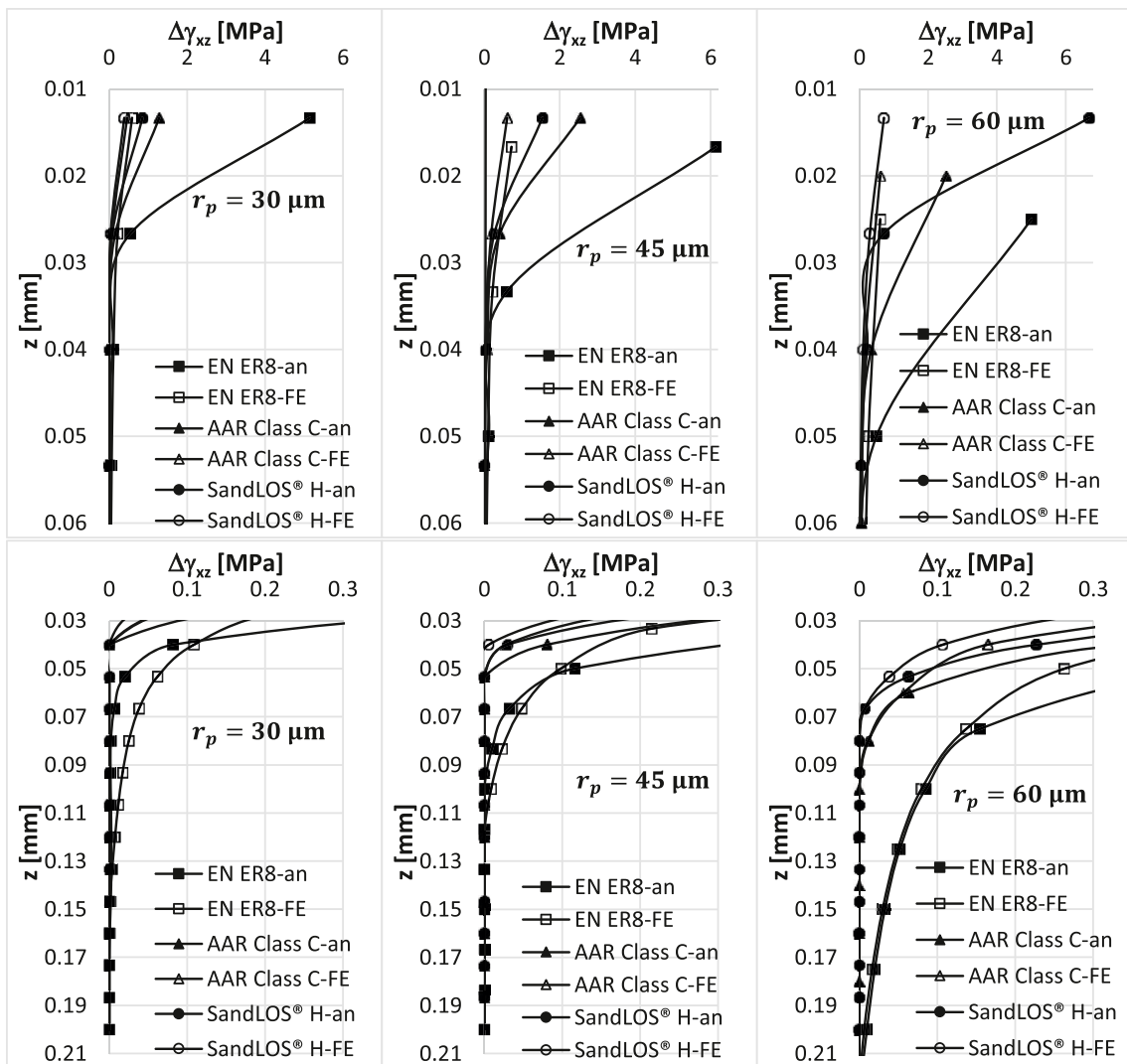

Fig. 9. Plastic strain increment at every cycle for the three materials and particle size, calculated with the analytical elastic pressure distribution (termination "-an" in the legends) and with the output distribution of the FE models with elastic-plastic materials (termination "-FE" in the legends). The upper diagrams show the strain field in the surface layer, the lower ones in the sub-surface layer.

Table 3

Input parameters assumed in the simulations of the rolling contact tests published in [2].

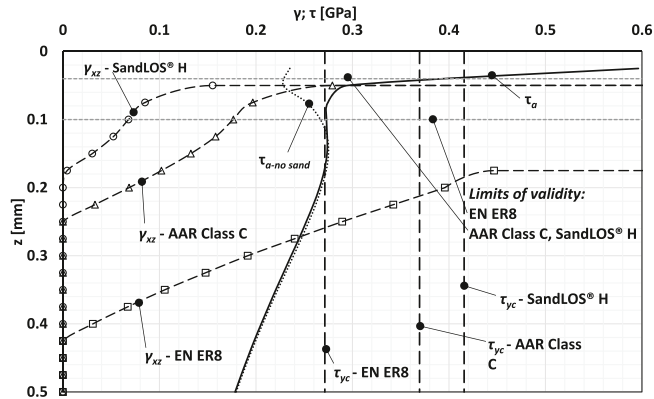| Nominal contact pressure [MPa]	Nominal contact width [mm]	Particle radius r_p [μm]	Particle spacing λ [μm]	Coefficient of friction f	Wear rate [mm/cycle]	Cycle number
1100	0.29	30	70	0.5	3×10^{-7}	1.3×10^5

Fig. 10. Plot of the applied alternated shear stress τ_a, the applied alternated shear stress calculated without solid contaminant $\tau_{a-no\ sand}$, the cyclic shear yield stress τ_{yc} of the three steels, the accumulated plastic shear strain γ_{xz} at the end of the simulation for the three steels.

the contact, meaning that the larger particles were broken into smaller ones during the contact. Therefore, this value was assumed as typical particle size. As the spacing λ is concerned, a value corresponding to particles very close to each other was assumed because the sand feed rate was very high in the experiments. The values of the input parameters related to the working conditions are reported in Table 3; the material properties assumed are the same as in the previous section, e.g. those reported in Table 2.

In Fig. 10, the results of the simulation are shown. The following quantities are plotted against the depth z:

- the applied alternated shear stress τ_a;
- the applied alternated shear stress calculated without solid contaminant $\tau_{a-no\ sand}$;
- the cyclic shear yield stress τ_{yc} of the three steels;
- the accumulated plastic shear strain γ_{xz} at the end of the simulation for the three steels.

In addition, the values of z below which the model cannot be considered accurate, according to the evaluation done in the previous section and in particular to the results shown in Figs. 8 and 9, are also mentioned as "Limits of validity".

Comparing the τ_a and $\tau_{a-no\ sand}$ it is evident that the two curves are overlapped below about 120 μm: this means that the field of influence of

the contaminant particle is limited to that depth, whereas below this depth the contact between the two discs dominates the stress field. Comparing the τ_a curves with the τ_{yc} curves of the three steels, for the AAR Class C and the SandLOS® H steels the applied stress exceeds the yield stress only in the layer of influence of the particles, whereas for the EN ER8 steel the τ_{yc} is exceeded even in the region of influence of the overall contact. In the curves of plastic strain γ_{xz} a region of huge ratcheting can be identified above the depth where the τ_{yc} is exceeded, recognizable by an almost null slope of the curve. This layer is within the region of influence of the particles for the AAR Class C and the Sand-LOS® H steels, whereas is much thicker for the EN ER8 steel.

Therefore, the model's validity extends below the superficial "strain-divergent" region for all examined materials. In fact, the numerical inaccuracies arising from using the analytical pressure distribution become physically meaningless when the model predicts a plastic strain that approaches infinity.

On the contrary, in the layer where the strain gradient is non-diverging ($z > 50\ \mu m$ for the AAR Class C and the SandLOS® H; $z > 180\ \mu m$ for the EN ER8), the model is accurate. These considerations show that the model results can be accepted for evaluating real cases, notwithstanding the approximation of the analytical contact pressure distribution.

This result is qualitatively consistent with the trend shown in the micrographs published in Ref. [2] and reported in Fig. 11: in those images, sections of the specimens in EN ER8 and improved AAR Class C (SandLOS® S), with the grain borders evidenced by Nital attack, are shown, and the layers characterized by high ratcheting are clearly visible. There is a significant difference in the thickness of this layer when compared with the calculated results, which can be imputed to the indeterminacy of many values used as input in the simulations, as well as to some physical phenomena (such as abrasion, sand embedding into the metal, etc.) which the model does not consider. However, the simulations explain the high strain depth difference between the softer EN ER8 and the harder AAR Class C.

Further considerations can be found if the interaction between crack propagation and wear are considered. As mentioned above, cracks can be supposed to be present where the critical strain of the material is exceeded by the calculated accumulated strain. The critical strain is a material property, but many studies showed that for railway wheel steels its value is of the order of 10. Looking at Fig. 10, the predicted crack depth is approximately equal to the thickness of the layer were strain tending to infinite are calculated. This corresponds to about 180 μm for the EN ER8 steel and to about 50 μm for the other steels, which are values rather consistent with the depth of the cracks shown in Fig. 11. As wear is considered in the simulations, the predicted crack
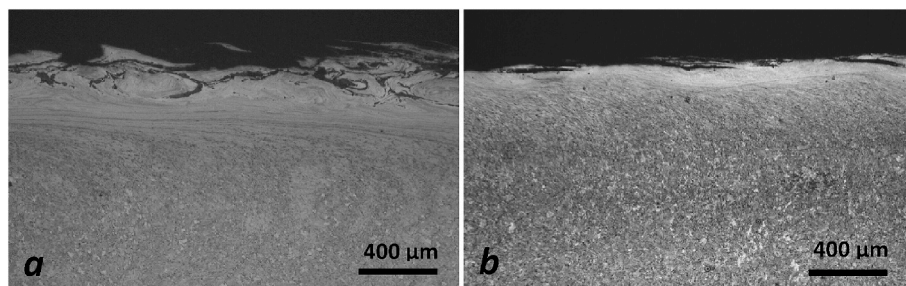

Fig. 11. Micrographs of the sections of the specimens in EN ER8 (a) and improved AAR Class C (b) with the grain borders highlighted using Nital attack [2].

Table 4
Input parameters assumed in the simulations of the rolling contact tests published in [18].

Nominal contact pressure [MPa]	Nominal contact half-width [mm]	Particle radius r_p [μm]	Particle spacing λ [μm]	Coefficient of friction f	Wear rate [mm/cycle]	Cycle number
1100	0.27	5–45	30–120	0.3	3×10^{-7}	5×10^4
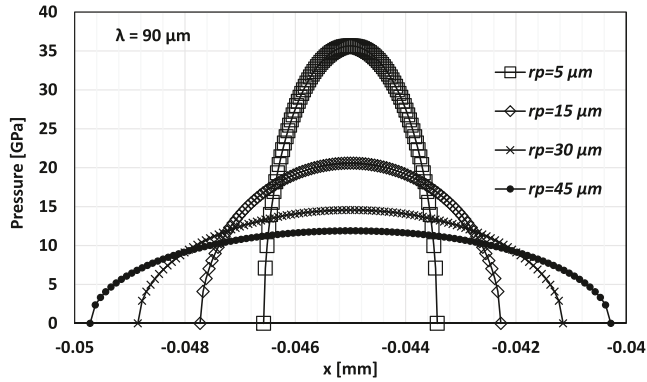
Fig. 12. Pressure distribution in the vicinity of one of the contaminant particles with varying particle size r_p, fixed particle spacing $\lambda = 90\ \mu m$, and other input parameters according to Table 4.

depth is the result of the interaction between wear and ratcheting.

3.2. Effect of the particle size and spacing

The second example of application is the test campaign done by Shi et al. [18] on discs machined from wheel steel CL60 and rail steel U71Mn, both of common use in China. In those experiments, various kinds of solid and liquid contaminants were used: commercial sand, with particle size ranging from 0.6 to 2 mm, under lubricated contact condition; various slurries obtained by mixing in different percentage of water with a pulverized sand, whose particle size ranged from 0.1 to 30 μm; dry and clean contact; contact lubricated with oil or water. The weight percentages of the solid fraction in the slurries were 0.5%, 5%, 25% and 50%. The main results they found about the topic of the present paper were:

- The adhesion coefficient was about 0.18 in lubricated contact, 0.3 in sand contaminated contact, 0.5 in dry clean contact, ranging from 0.2 to 0.35 in slurry contaminated contact, increasing with the percentage of pulverized sand in the slurry;
- The wear rate was the lowest in clean lubricated contact; it increased with the percentage of the pulverized sand in the slurry contaminated contact; it was the highest in the sand contaminated contact. In the clean dry contact the wear rate was approximately averaged between the lowest and the highest one;
- The depth of the layer interested by severe ratcheting was higher in dry condition, both clean and with sand, than in slurry-contaminated contact; considering the tests with the slurry, the ratcheting depth increased with increasing the pulverized sand fraction in the slurry.

Overall, both ratcheting and wear increased with particle size, adhesion coefficient and particle concentration.

Simulations in the conditions shown in Table 4 were carried out to investigate the effect of particle size and spacing. The wheel material properties were assumed as equal to those of the EN ER8 steel (see Table 2) because the two steels have similar hardness. Average values for coefficient of friction and wear rate were taken from the experimental test data to isolate the influence of the contaminant geometric parameters. The number of cycles was the same as in the tests. The
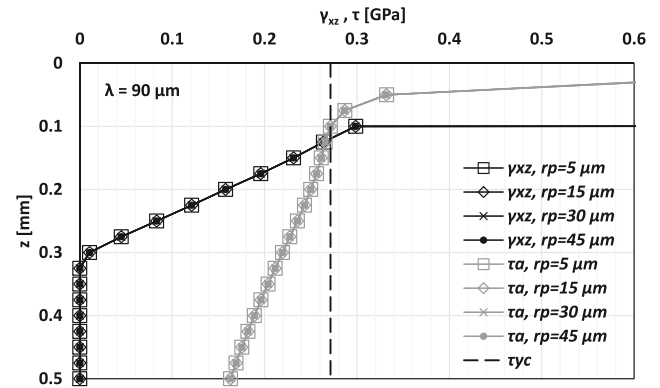
Fig. 13. Accumulated plastic strain along the depth z in the simulations, with varying particle size r_p, fixed particle spacing $\lambda = 90\ \mu m$, and other input parameters according to Table 4.
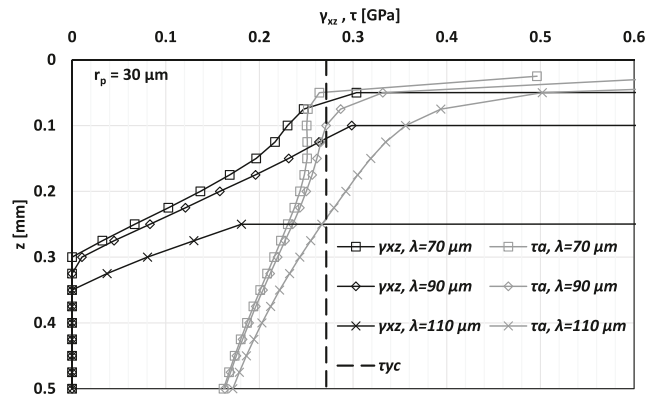
Fig. 14. Accumulated plastic strain along the depth z in the simulations, with fixed particle size $r_p = 30\ \mu m$, varying particle spacing λ, and other input parameters according to Table 4.

particle size ranged from the typical value of the pulverized sand in the slurry to a value larger than that of survived (non-crushed) particles.

First, simulations with varying particle size and fixed particle spacing $\lambda = 90\ \mu m$ were done. Fig. 12 shows the pressure distribution in the vicinity of a contaminant particle. As the particle size increases, the pressure peak decreases, and the contact width increases. However, this has no significant effect on the stress and strain field at depths below the minimum value ($z = 25\ \mu m$) considered in the simulations.

In fact, looking at Fig. 13, the curves of both accumulated plastic strain γ_{xz} and applied alternated shear stress τ_a don't depend on the particle size. Again, a layer of huge ratcheting is predicted in the surface layer where τ_a exceeds the cyclic shear yield stress τ_{yc}.

Fig. 14 shows the accumulated plastic strain γ_{xz} and the alternated shear stress τ_a with fixed particle size $r_p = 30\ \mu m$ and varying particle spacing λ. The results show that by increasing the particles spacing, and consequently decreasing the number of particles simultaneously entrapped in the contact region, the layer of high ratcheting increases. This can be explained by the fact that as far as the number of particles decreases, the local force at the body-particle interface increases,
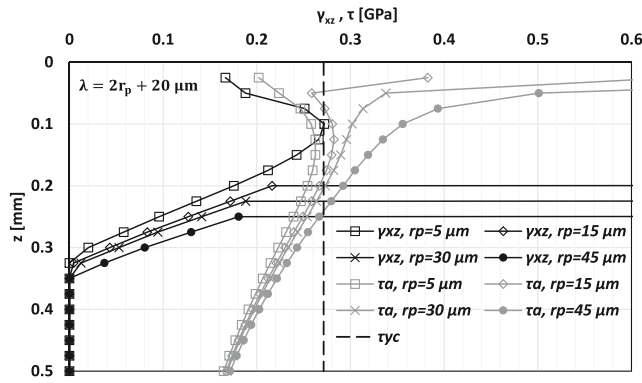
Fig. 15. Accumulated plastic strain along the depth z in the simulations, with varying particle size r_p and proportionally varying particle spacing λ, and other input parameters according to Table 4.

Table 5
Evaluation of the points of strength and weakness of the model emerging from the comparison with published results.

	Points of strength	Point of weakness
Faccoli et al. [2]	- Effect of the material strength well captured -Prediction of the crack depth consistent	-Consistency of the plasticized depth only qualitative
Shi et al. [18]	-Effect of particle spacing identified as a crucial parameter for ratcheting -Effect of particle size well captured for macroscopic differences between the particles	-Effect of particle spacing not well captured in case of slurries with pulverized solid contaminant

therefore increasing the thickness of the layer where high ratcheting occurs. This observation is evident even comparing the τ_a profile with the cyclic shear yield stress τ_{yc}.

This suggests that the reason why in Ref. [18] wear and ratcheting were higher with the commercial sand than in the cases with the slurries is related to the particle spacing rather than to the particle size. Indeed, the larger the particle size, the lower the number of particles that can be simultaneously entrapped in the contact region. To verify this, simulations with increasing particle size and with spacing $\lambda = 2r_p + 20\ \mu m$ (so that the minimum distance between the external borders of the particles was 20 μm) were done; the number of entrapped particles ranged from 18 with $r_p = 5\ \mu m$ to 4 with $r_p = 45\ \mu m$.

Fig. 15 shows the results: with $r_p = 5\ \mu m$ no ratcheting is predicted: only an initial plasticization that does not accumulate is obtained. As far as the particle size increases and, consequently, the particle number decreases, ratcheting occurs involving an increasing depth.

These results explain why, in Shi et al.'s [18] experiment, ratcheting increased passing from the slurry to the sand contamination. However, they do not explain why ratcheting increased with increasing the pulverized sand fraction in the slurry: indeed, according to Fig. 14, they should have decreased owing to the decrease of the particle spacing with constant particle size. This is a limitation of the model, which can simulate the phenomena correlated with ratcheting, but other interacting mechanisms are not allowed. In particular, abrasion could significantly affect the slurry contaminated contact. Abrasion is due to the particles that scratch the surface of the bodies and is not related to the local pressure at the contact between the bodies and the particles; it is instead an indentation mechanism of the particles on the surfaces of the bodies. Therefore, on the one hand the increase of the particle number reduces the effects of the local pressure peaks; on the other hand, it increases the abrasive mechanisms. Shi et al. [18] found that ratcheting and wear were much higher in the wheel material, despite it was harder than the rail one: this is a clue of the two-body abrasion, which is due to the particles that are embedded in the softer material and scratch the harder one. In tests with commercial sand, characterized by larger particles, abrasion is supposed to be less critical because embedding the particles in the rail specimen is less easy. In this condition, the results of the present model are expected to be more representative of the real interaction mechanism.

4. Conclusions

A fast numerical method was developed to simulate ratcheting in solid-contaminated wheel-rail contact. The model is based on simplifying hypotheses: in particular, an analytical contact pressure distribution is used, which is obtained by a theory based on linear elastic material for the main contacting bodies.

To evaluate the error, finite element models with elastic-plastic materials for the wheel and rail bodies were built, and the pressure obtained were used as input for the proposed numerical method. Comparing the results obtained with such distributions with those obtained with the analytical pressure distribution, it was seen that the error is generally confined in a very shallow layer, comparable to the size of the particles, and it decreases as far as the material strength and particle size increase. It was shown that, below a certain depth, the influence of the shape of the local pressure distribution at the body-particle interface is negligible.

The effectiveness of the proposed method was assessed by simulating ratcheting in two cases of experimental tests previously published, one with varying wheel materials, the other with varying contaminant characteristics. In both cases, the model was able to identify the depth of the layer where plastic strain was mainly influenced by the local pressure peaks at the particle-body interface. The comparison with the published results allowed identifying, in both cases, the points of strength and weakness of the model, which are summarized in Table 5.

Despite some quantitative differences between the predicted and observed results, which were attributed to the model approximations and the indeterminacy of some input parameters, the model provided qualitative explanations of the observed phenomena, highlighting the role of the involved parameters in the plastic strain accumulation. The model loses effectiveness when phenomena other than ratcheting and wear are involved, such as the concurrent presence of liquid and solid contaminants that triggers fluid-driven crack propagation which is not currently included in the model.

From this evaluation it can be concluded that the proposed model can be a useful comparative tool for evaluating the material responses when ratcheting is the main damage phenomenon in a solid contaminated environment. This is the case, for instance, of wheels operating in sandy environments or with sanding systems, where ratcheting and wear are the dominant mechanisms. The proposed model allows estimating the depth interested by extreme ratcheting and cracking, this way allowing the most appropriate material choice.

CRediT authorship contribution statement

Angelo Mazzù: Conceptualization, Data curation, Formal analysis, Investigation, Methodology, Supervision, Validation, Visualization, Writing – original draft, Writing – review & editing. **Davide Battini:** Conceptualization, Formal analysis, Investigation, Validation, Writing – review & editing. **Nicola Zani:** Conceptualization, Formal analysis, Investigation, Visualization, Writing – review & editing.

Declaration of competing interest

The authors declare that they have no known competing financial interests or personal relationships that could have appeared to influence the work reported in this paper.

Data availability

Data will be made available on request.

References

[1] L. Bruno, M. Horvat, L. Raffaele, Windblown sand along railway infrastructures: a review of challenges and mitigation measures, J. Wind Eng. Ind. Aerod. 177 (2018) 340–365.

[2] M. Faccoli, C. Petrogalli, M. Lancini, A. Ghidini, A. Mazzù, Effect of desert sand on wear and rolling contact fatigue behaviour of various railway wheel steels, Wear 396–397 (2018) 146–161.

[3] K. Shu, W.J. Wang, E. Meli, H.H. Ding, Z.Y. Han, M. Zou, Q.Y. Liu, Study on the influence of sand erosion process on the wear and damage of heat-treated U75V rail steel, J. Tribol. 143 (2021) 081703.

[4] O. Arias-Cuevas, Z. Li, R. Lewis, E.A. Gallardo-Hernández, Laboratory investigation of some sanding parameters to improve the adhesion in leaf-contaminated wheel—rail contacts, Proc. Inst. Mech. Eng. F J. Rail Rapid Transit 224 (3) (2010) 139–157.

[5] W.A. Skipper, A. Chalisey, R. Lewis, A review of railway sanding system research: adhesion restoration and leaf layer removal, Tribol. Mater. Surface Interfac. 12 (4) (2018) 237–251.

[6] K. Ishizaka, S.R. Lewis, R. Lewis, The low adhesion problem due to leaf contamination in the wheel/rail contact: bonding and low adhesion mechanisms, Wear 378–379 (2017) 183–197.

[7] N. Zani, C. Petrogalli, Predictive maps for the rolling contact fatigue and wear interaction in railway wheel steels, Wear 510–511 (2022) 204513.

[8] C. Wang, L.B. Shi, H.H. Ding, R. Galas, J. Guo, Q.Y. Liu, Q.Y. Liu, Z.R. Zhou, M. Omasta, Adhesion and damage characteristics of wheel/rail using different mineral particles as adhesion enhancers, Wear 477 (2021) 203796.

[9] O. Arias-Cuevas, Z. Li, R. Lewis, A laboratory investigation on the influence of the particle size and slip during sanding on the adhesion and wear in the wheel–rail contact, Wear 271 (2011) 14–24.

[10] Y. Lyu, Y. Zhu, U. Olofsson, Wear between wheel and rail: a pin-on-disc study of environmental conditions and iron oxides, Wear 328–329 (2015) 277–285.

[11] Zhou, Y., Peng, J. F., Wang, W. J., Jin, X. S., and Zhu, M. H., "Slippage effect on rolling contact wear and damage behavior of pearlitic steels", Wear, 362–363, pp 78-86.

[12] W.J. Wang, H.F. Zhang, H.Y. Wang, Q.Y. Liu, M.H. Zhu, Study on the adhesion behavior of wheel/rail under oil, water and sanding conditions, Wear 271 (2011) 2693–2698.

[13] M. Omasta, M. Machatka, D. Smejkal, M. Hartl, I. Křupka, Influence of sanding parameters on adhesion recovery in contaminated wheel–rail contact, Wear 322–323 (2015) 218–225.

[14] R. Lewis, R.S. Dwyer-Joyce, Wear at the wheel/rail interface when sanding is used to increase adhesion, Proc. Inst. Mech. Eng. F J. Rail Rapid Transit 220 (1) (2006) 29–41.

[15] W. Huang, X. Cao, Z. Wen, W. Wang, Q. Liu, M. Zhu, X. Jin, A subscale experimental investigation on the influence of sanding on adhesion and rolling contact fatigue of wheel/rail under water condition, ASME. Journal of Tribology 139 (1) (2017) 011401.

[16] D.G. Grieve, R.S. Dwyer-Joyce, J.H. Beynon, "Abrasive wear of railway track by solid contaminants, Proc. Inst. Mech. Eng. F J. Rail Rapid Transit 215 (2001) 193–205.

[17] E.A. Gallardo-Hernández, R. Lewis, Twin disc assessment of wheel/rail adhesion, Wear 265 (2008) 1309–1316.

[18] L.B. Shi, C. Wang, H.H. Ding, D. Kvarda, R. Galas, M. Omasta, W.J. Wang, Q.Y. Liu, M. Hartl, Laboratory investigation on the particle-size effects in railway sanding: comparisons between standard sand and its micro fragments, Tribol. Int. 146 (2020) 106259.

[19] A. Mazzù, A. Ghidini, N. Zani, M. Faccoli, A simplified numerical study of wheel/rail material coupling in presence of solid contaminants, Tribol. Mater. Surface Interfac. 15 (2) (2021) 102–114.

[20] A. Mazzù, A. Ghidini, N. Zani, M. Faccoli, Study of wheel/rail material coupling in presence of solid contaminants. Proceedings of 11th International Conference on Contact Mechanics and Wear Rail/Wheel Systems, Delft, Netherlands, 2018, pp. 701–710.

[21] A. Mazzù, D. Battini, A model for the assessment of wheel–rail contact in the presence of solid contaminants, Tribol. Trans. 62 (2) (2019) 230–238.

[22] A. Mazzù, A simplified non-linear kinematic hardening model for ratchetting and wear assessment in rolling contact, J. Strain Anal. Eng. Des. 43 (5) (2008) 349–360.

[23] A. Mazzù, Surface plastic strain in contact problems: prediction by a simplified non-linear kinematic hardening model, J. Strain Anal. Eng. Des. 44 (3) (2009) 187–199.

[24] L. Shi, D. Wang, K. Li, Windblown sand characteristics and hazard control measures for the Lanzhou–Wulumuqi high-speed railway, Nat. Hazards 104 (2020) 353–374.

[25] S.R. Lewis, S. Riley, D.I. Fletcher, R. Lewis, Optimisation of a railway sanding system for optimal grain entrainment into the wheel-rail contact, Proc. Inst. Mech. Eng. F J. Rail Rapid Transit 232 (2018) 43–62.

[26] V. Bhargava, G.T. Hahn, C.A. Rubin, An elastic-plastic finite-element model of rolling-contact, Part 1: analysis of single contact, Journal of Applied Mechanics-Transactions of the ASME 52 (1) (1985) 67–74.

[27] V. Bhargava, G.T. Hahn, C.A. Rubin, An elastic-plastic finite-element model of rolling-contact, Part 1: analysis of repeated contacts, Journal of Applied Mechanics-Transactions of the ASME 52 (1) (1985) 75–82.

[28] A. Mazzù, C. Petrogalli, M. Faccoli, An integrated model for competitive damage mechanisms assessment in railway wheel steels, Wear 322–323 (2015) 181–191.